Effects of Kinetic Ballooning Modes on the electron distribution function in the core of high-performance tokamak plasmas

S. Mazzi, G. Giruzzi, Y. Camenen, R. Dumont, M. Fontana, E. de la Luna, F.P. Orsitto, L. Senni, K. Aleynikova, S. Brunner, et al.

Effects of Kinetic Ballooning Modes on the electron distribution function in the core of high-performance tokamak plasmas

S. Mazzi[1,*], G. Giruzzi[1], Y. Camenen[2], R. Dumont[1], M. Fontana[3], E. de la Luna[4], F. P. Orsitto[5], L. Senni[5], K. Aleynikova[7], S. Brunner[8], B. J. Frei[9], J. Garcia[1], A. Zocco[7], D. Frigione[5], L. Garzotti[10], F. Rimini[10], D. van Eester[11], JET contributors[a], and EUROfusion Tokamak Exploitation Team[b]

[1]CEA, IRFM, F-13108 Saint-Paul-lez-Durance, France
[2]Aix-Marseille Université, CNRS PIIM, UMR 7345 Marseille, France
[3]United Kingdom Atomic Energy Authority, Culham Centre for Fusion Energy, Culham Science Centre, Abingdon, Oxon, OX14 3DB, UK
[4]National Fusion Laboratory, CIEMAT, Madrid, Spain
[5]ENEA Department Fusion and Technology for Nuclear Safety, C.R. Frascati, 00044 Frascati, Italy
[6]Istituto per le Applicazioni del Calcolo "Mauro Picone" Consiglio Nazionale delle Ricerche (CNR), Via dei Taurini 19, 00185, Rome, Italy
[7]Max-Planck-Institut fur Plasmaphysik, EURATOM Association, Greifswald, Germany
[8]Ecole Polytechnique Fédérale de Lausanne (EPFL), Swiss Plasma Center (SPC), Lausanne, Switzerland
[9]Max Planck Institute for Plasma Physics Boltzmannstr 2 85748 Garching Germany
[10]UKAEA, Culham Centre for Fusion Energy, Abingdon, United Kingdom of Great Britain and Northern Ireland
[11]Laboratory for Plasma Physics, LPP-ERM/KMS, TEC Partner, 1000 Brussels, Belgium
[a]See the author list of C. F. Maggi 2024 Nucl. Fusion in press https://doi.org/10.1088/1741-4326/ad3e16
[b]See the author list of "Overview of the EUROfusion Tokamak Exploitation programme in support of ITER and DEMO" by E. Joffrin Nuclear Fusion 2024 10.1088/1741-4326/ad2be4
[*]email: samuele.mazzi@cea.fr

Abstract

This article is dedicated to study the physical causes of a long-standing issue experienced in different tokamak devices throughout the last decades: the observed discrepancies between Electron Cyclotron Emission (ECE) and Thomson Scattering (TS) diagnostic measurements at high temperature in the core tokamak plasmas. A recently developed heuristic model [M. Fontana *et al.*, *Phys. Plasmas* **30**, 122503 (2023)], tested on an extensive data set from multiple pulses in the frame of recent JET campaigns, showed that such ECE-TS discrepancy could be reconciled by introducing a bipolar perturbation in the electron distribution function. Such a perturbation indeed modifies the EC emission and absorption spectra. Nonetheless, the heuristic model does not provide the physical mechanisms causing such a bipolar perturbation. In this work, detailed gyrokinetic analyses unveil the unexplored wave-particle interaction between electrons and the Kinetic Ballooning Modes (KBMs) in tokamak plasmas. The numerical studies of the core of a selected high-temperature pulse of the JET device revealed that the electron-β was large enough to destabilize KBMs. Such KBMs affect the electron distribution function in momentum space with a characteristic bipolar structure. The position of the bipolar structure in the velocity space is intimately linked to the electron diamagnetic frequency. The amplitude of the perturbation, assessed through nonlinear computations, is shown to be dependent on the amplitude of the KBM-induced turbulent fluxes. Thus, this study demonstrates that KBMs, destabilized by the high-β plasma conditions achieved in the core of high-temperature scenarios, perturb the electron distribution function forming bipolar structures in momentum space and, thereby, modifying the EC spectrum. Therefore, the reported mechanism may represent an intriguing explanation of the ECE-TS measurement discrepancy in the deep core of high-temperature plasmas.

1 Introduction

In future fusion reactors, where the bulk plasma temperature is expected to be higher than 10 keV, the exact measurement of the electron temperature T_e is crucial to diagnose the plasma characteristics and to determine the performance of the device. Yet, the long-standing issue of discrepancy between the most commonly used diagnostics for measuring T_e in current tokamaks, i.e. the electron cyclotron emission (ECE) [1] and the Thomson Scattering (TS) [2], may complicate the evaluation of such measurements. Indeed, in different

tokamaks since the early 1990s, the temperature measured by the ECE and TS presented a noteworthy difference at high-temperature plasma conditions.

Differences were observed in many devices in the last 30 years, among them TFTR [3, 4] and JET [5] have been among the first where the ECE-TS discrepancy in the plasma core was measured when $T_e \gtrsim 5$ keV. In those cases, the ECE temperature was systematically observed to be larger than the TS one by up to 20%, well beyond the error bars. Interestingly, also the temperature of the 2^{nd} and 3^{rd} harmonics of the eXtraordinary (X) mode in JET resulted in considerable discrepancies [5], even though for high temperature and sufficiently large optical depth the two should yield the same measurement. A possible explanation could be that the electron distribution function presented some non-Maxwellian features in the plasma deep-core [6]. Indeed, the ECE measurements are very sensitive to the precise shape of the electron distribution function in the energy space [7], while the TS is much less [8], and therefore the difference could be due to the non-Maxwellian shape of the distribution function.

Some attempts to reproduce this discrepancy have been carried out in some dedicated JET experiments in the subsequent years [9]. Similar studies in Alcator C-Mod showed that no ECE-TS discrepancy was observed even when $T_e = 8$ keV plasmas were achieved [10], likely implying that high temperatures are not the only requirement to detect the ECE-TS discrepancy.

Thus, in order to understand similar behaviour could be expected also in next-generation fusion devices, such as ITER, expected to operate at bulk temperatures up to 30 keV and understand its physical cause, a rich database of JET pulses from experimental campaigns spanning the years from 2019 to 2022, with more than 250 pulses and 14000 samples of ECE vs. TS measurements at the same time instants [11, 12], has been built. Among such pulses, in which high-performances, and thereby high-temperature, plasma conditions have been achieved, plasmas from the Deuterium-Tritium DTE2 JET campaign [13] are also included. In this database, where plasma scenarios with different heating systems, and broadly different heating power, are included, it is clear that the ECE-TS discrepancy is retrieved [11, 12]. Thus, it has been possible to systematically apply a recently developed heuristic model with an ad-hoc bipolar perturbation of the electron distribution function to such a database [14]. This has unveiled that, depending on the plasma scenario, the ECE temperature measurements can be successfully recovered by using such an ad-hoc perturbation, with bipolar shape and appropriate parameters [12].

Although this is a crucial step towards the solution of such a long-standing issue, the heuristic model does not explain the physical causes leading to the bipolar perturbation in the electron distribution function which is necessary to match the experimental results. Some preliminary analyses pointed out that the collisional relaxation of fusion-born alpha particles on the electrons could perturb their distribution with a bipolar structure at the electron thermal velocity [15]. In this work, instead, the analysis focuses on the effects of specific micro-instabilities, destabilized in the deep-core of these high-temperature JET plasmas, on the local electron distribution function. Indeed, in these high-temperature plasma conditions, the β parameter, that is the ratio between the kinetic and the magnetic pressure, can be large enough to drive unstable the so-called Kinetic Ballooning Modes (KBMs) [16, 17].

In Section 2, the experimental observations of ECE-TS measurement discrepancy at high plasma core temperature in the analyzed JET experimental campaigns are introduced and the database built upon such observations is described. The bases of the recently developed heuristic model able to reconcile and explain the ECE-TS discrepancy through the introduction of a bipolar perturbation in the electron distribution function are also presented. Eventually, before the conclusions are drawn in Section 4, the main part of the manuscript is exhaustively discussed in Section 3: the gyrokinetic code employed in this work is firstly introduced and then the stability of the selected JET pulse is analyzed, with a particular focus on the effect of the Kinetic Ballooning Mode (KBM) instability on the perturbed electron distribution function and on the physical causes leading to such perturbation; then advanced nonlinear analyses assess the amplitude and the secular presence of the KBM-induced perturbation, together with some insights on possible energy transfers caused by such interplay.

2 Experimental observations of T_e measurement divergence reconciled through ad-hoc perturbations of the electron distribution function

In this section, the relevant aspects of the background studies which have motivated the work of this manuscript are given. For more details on the broad and comprehensive analyses, the reader is addressed to Refs. [11, 12].

A large database, of more than 1400 samples from around 250 pulses, has been recently built to compare the radiative temperature measured by the ECE diagnostic T_{ECE} and the electron temperature measured by

the Thomson Scattering diagnostic T_{TS} in the core of JET plasmas [11,12]. In order to avoid possible spatial discrepancies between the lines of sight of the two different diagnostics, and also to weaken uncertainties in the plasma position, the temperatures T_{ECE} and T_{TS} have been averaged in the radial region 2.85−3.15 m, i.e. around ±15 cm with respect to the magnetic axis (located at ~ 3 m).

Such a database includes pulses from the experimental campaigns performed in the years from 2019 to 2022, therefore considering a rich variety of different plasma scenarios, with diverse plasma currents, toroidal magnetic field amplitudes and external heating systems, performed not only in D-D plasma mixture, but also in D-T within the DTE2 JET experimental campaign [13].

In spite of the heterogeneity of the pulses making up the database, it could be observed that at high temperatures, that are for $T_{TS} \gtrsim 5$ keV, there is a large dispersion of the measurements, and in particular a discrepancy between the temperature measured with the two diagnostics. Both $T_{TS} > T_{ECE}$ and $T_{ECE} > T_{TS}$ have been found in this JET database. This statistical observation is partly consistent with the results reported in earlier studies at JET [5] and TFTR [3,4], where the radiative temperature measured by the ECE was larger than the TS-measured one, when $T_{TS} > 5$ keV. In these previous studies, it was already speculated that the discrepancy could have been traced back to the presence of particular perturbation in the electron distribution function, which departed therefore from the expected Maxwellian shape [6]. Such a perturbation in the electron distribution function was shown theoretically to lead to strong difference in the measured radiative temperature by the ECE [7]. Since the TS diagnostic is not strongly sensitive to small perturbations in the electron distribution function [8], the difference in the diagnostic principles could be the underlying cause leading to the long-standing issue of the ECE-TS discrepancy.

Therefore, in order to reconcile the ECE and the TS measured temperatures of this broad JET database, an heuristic model has been developed. For more details on this heuristic model, as well as on the analytical interpretation of the radiative temperature measured by the ECE, the reader can refer to [14,18].

The principle of this heuristic model is to add a fairly localized perturbation to a Maxwellian distribution function and then to determine the radiative temperature that should be measured by the ECE diagnostic.

Starting from a Maxwellian distribution function F_M, it is possible to add an arbitrary perturbation f_1 to it with diverse shapes, as well as different amplitudes f_0, extensions δ_0 and centered positions p_0 along the total momentum p space. Although the choices of this perturbation are possibly infinite, in the following the focus will be only put to an isotropic sinusoidal-shaped perturbation:

$$f_1(p) = f_0 \sin\left(\frac{\pi}{\delta_0}(p - p_0)\right) \tag{1}$$

An example of such a perturbation for a selected pulse of the JET database is shown in panel (b) of Figure 1.

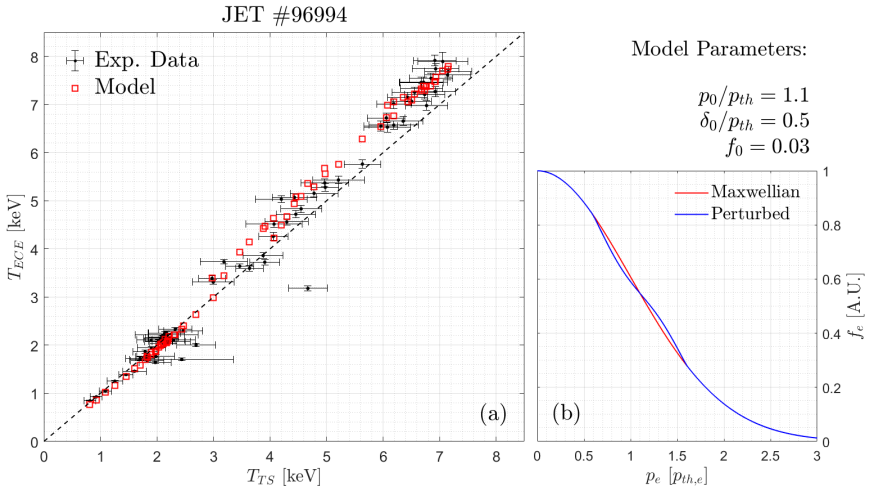

Figure 1: In panel (a), the experimental measurements of the ECE and TS diagnostics for the selected JET pulse #96994 are displayed with filled points. With open circles, the recalculated ECE temperature considering a perturbed distribution function with a sinusoidal centered at $p_0 = 1.1 p_{th}$, with an extension of $\delta_0 = 0.5 p_{th}$ and with an amplitude of $f_0 = 0.03$, is shown. In panel (b) the total electron distribution function f_e is displayed with (in blue) and without (in red) the employed perturbation f_1 along the total electron momentum p_e.

In this work, we limit ourselves to investigate about the origin of such a perturbation, with a first verification study on the selected JET pulse #96994, which was part of an earlier study on the development

of an H-mode regime with small-amplitude and high-frequency edge localized modes (ELM), named Baseline Small ELM (BSE) regime [19]. This choice is motivated by the high-performance obtained in such a JET pulse and by the simultaneous availability of ECE and TS measurements in the plasma core. In particular, this pulse has been analyzed in detail and a noteworthy discrepancy between the ECE and TS measurements has been highlighted [11, 12], which has been reconciled by adding specific perturbation to the electron distribution function [14]. For this pulse, the added perturbation is centered at $p_0/p_{th} = 1.1$, with an extension of $\delta_0/p_{th} = 0.5$ and an amplitude of $f_0/F_M = 0.03$. In panel (b) it is possible to see that such a perturbation, added to the equivalent Maxwellian, allows to remarkably match the ECE measurements of this pulse accurately, which clearly deviates from the temperature measured by the TS diagnostic.

3 Gyrokinetic analyses of a selected JET core plasma

Several mechanisms can be responsible of a perturbation of the electron distribution function in magnetized plasmas, among them the relaxation of specific instabilities on the electron distribution through specific physical mechanisms could be mentioned. This has been observed, e.g., in the magnetosheath: signatures of Kinetic Alfvén Waves (KAW) damping on the electron distribution function through a Landau damping mechanism. This has been experimentally demonstrated through advanced field-particle correlation techniques [20], and later also verified by in-depth gyrokinetic analyses [21]. Nevertheless, other possible mechanisms, such as resonant interaction between specific instabilities and characteristic particle motion frequency, must be considered and examined. Motivated by such considerations and by the systematic ECE-TS measurement discrepancy at high plasma temperature, we have performed gyrokinetic numerical studies of radially localized instabilities in the core plasma of the selected JET pulse #96994, which is included in the database presented in Section 2. Indeed, as already pointed out, the discrepancy between the ECE and TS measurements is mainly observed in a limited region of the plasma, $\sim \pm 15$ cm around the magnetic axis. Therefore, specific unstable modes with narrow structure may be suitable candidates perturbing the electron distribution function in high-performance core plasmas.

3.1 Modelling setup

In this work, we have made use of the GENE code [22] in its flux-tube version. By evolving the perturbed particle distribution functions δf_s in five dimensions and self-consistently with the time evolution of the electrostatic and magnetic potentials (ϕ and A), the GENE code allows to determine the impact of radially localized instabilities on the electron distribution function in physical conditions highly relevant for the JET core plasmas. The five dimensions are represented by the three spatial directions, which are the radial x, the parallel to the magnetic field z and the binormal y, and by the two in the velocity space, i.e. the component of the velocity parallel to the magnetic field $v_\parallel$ and the magnetic moment μ. In the following, the radial and the binormal directions are also indicated with the respective wavenumbers k_x and k_y, since the periodic boundary conditions in the perpendicular domain of the simulated region, which are an inherent condition of the flux-tube approximation, allow a spectral approach along such directions. The GENE code employs the so-called δf splitting, by evolving only the perturbed part δf of the distribution function and considering a static equilibrium distribution function F_M, with the constraint of $\delta f \ll F_M$ [22]. In the remainder of the manuscript, thus, the notations δf and F_M represent the perturbed and the equilibrium parts of the distribution function, respectively. Thus, the total electron distribution function, as displayed in Figure 1(b), can be expressed as $f_e = F_M + \delta f_e$. Moreover, in order to be consistent with the heuristic model developed in Refs. [12, 14], the distribution function will be mainly shown in momentum space instead of the velocity space.

Within this framework, we have analyzed the plasma core of JET pulse #96994. The chosen flux-tube is centered at $\rho_{tor} = 0.15$ (where ρ_{tor} is the square root of the normalized toroidal magnetic flux), corresponding to around 13 cm of distance from the magnetic axis, and thereby falling within the region of interest [11, 12]. In this way, we are considering plasma conditions close to those at which the ECE-TS discrepancies are significant, taking also into account not to depart excessively from the experimentally reliable measurements. Also for this reason, the input parameters, reconstructed through the CRONOS suite of integrated modelling [23], have been scanned around the experimental values, taking into account the error bars. Table 1 summarizes the relevant input parameters of the gyrokinetic simulations. The modelling setup has been accurately chosen and convergence studies have been performed both linearly and nonlinearly. Thus, the employed numerical resolution in the nonlinear simulation is $(n_{k_x}, n_{k_y}, n_z, n_{v_\parallel}, n_\mu) = (680, 112, 24, 36, 32)$, with the minimum considered binormal wavenumber $k_{y,min}\rho_s = 0.011$ (corresponding to the toroidal mode number $n = 1$) and the maximum radial wavenumber $k_{x,max}\rho_s = 3.15$, where ρ_s is the thermal ion Larmor radius at the sound speed. Two species are employed, kinetically treated electrons and thermal ions (Deuterium). The fast ions have also been introduced in particular linear simulations, but were

Table 1: Plasma parameters considered in GENE simulations modelling JET pulse #96994 at $\rho_{tor} = 0.15$ and $t \approx 10$ s. Here n represents the species density, $R/L_{n,T}$ the logarithmic density and temperature gradient normalized to the major radius R, β_e the electron-beta, and $\nu^* \equiv (an_e/4|e|^2 n_i)\nu_{ei}$ the normalized collision frequency, where a is the minor radius, e the electron charge and ν_{ei} the Hinton-Hazeltine electron-ion collision rate [26]. Eventually, the normalization factors in standard units are also reported, i.e. the on-axis magnetic field strength B_0, the local electron temperature T_e and density n_e, and the major R and minor a radii.

q	$\hat{s}$	T_i/T_e	n_D/n_e	R/L_n	R/L_{T_e}	R/L_{T_i}
1.05	0.10	1.42	1	1.71	2.94	2.11
β_e [%]	ν^*	B_0 [T]	T_e [keV]	n_e [m^{-3}]	R [m]	a [m]
2.92	$0.66 \cdot 10^{-4}$	2.81	6.78	$8.44 \cdot 10^{19}$	3.24	0.93

not considered in the nonlinear calculations. Realistic magnetic geometry and collisions have been retained in the simulations. For the magnetic geometry we made use of the Miller parametrization [24], while for the collisions a Landau-Boltzmann operator is chosen [25]. In some specific simulations, highlighted in the following, the simplified geometry $\hat{s} - \alpha$ is employed in order to match theoretically-derived expressions. The impurity species have been neglected due to their low concentration in the core. Although with a low value, consistently with the experimentally-constrained results of the integrated modelling, the flow shears derived by the plasma rotation have been included in specific linear simulations.

3.2 Linear simulation results

In Figure 2, the linear spectra of JET pulse #96994, at the time $t = 10$ s, i.e. during the flat-top phase, at $\rho_{tor} = 0.15$ computed by GENE are shown for different values of the ion temperature gradient R/L_{T_i}. The nominal value of the ion temperature gradient is 2.11, but large uncertainties are present due to the lack of T_i experimental measurements in this core region. This justifies the broad scan that has been performed. Two different instability branches are visible in the low-k_y region of the linear spectra, both with positive diamagnetic drift rotation ($\omega > 0$) that in GENE convention is representative of the ion drift direction. These instabilities are identified as Kinetic Ballooning Modes (KBMs), already found unstable in previous analyses of core JET plasmas in hybrid scenarios [27, 28]. The ballooning structures of two different, representative eigenmodes, i.e. $k_y\rho_s = 0.022$ and $k_y\rho_s = 0.224$, are reported in Figure 3. For more details on the ballooning representation, the reader can refer to the seminal works Refs. [29, 30]. Strongly elongated structures in the ballooning space, thereby along the magnetic field line, correspond to radially localized structures in the real space. This consideration indicates that the effect of such instabilities may be localized to the region of interest. It should also be noted that the elongated structures observed in Figure 3 are similar to those reported for earlier JET core studies in low magnetic shear plasma conditions (Refs. [27, 28]). To further corroborate the identification of these unstable modes, it could be observed that for both wavevectors the real and imaginary components of the vector potential have a clear out-of-phase symmetry ($\mathbf{Re}[A_\parallel] \propto -\mathbf{Im}[A_\parallel]$), which is a signature of the KBM instability [31]. Moreover, the critical MHD $\beta_{e,crit} = 0.6\hat{s}/[q_0^2(2R/L_n + R/L_{T_e} + R/L_{T_i})]$ [32] for the nominal input parameters of this JET case is $\beta_{e,crit} = 0.6\%$, much less than the employed value of $\beta_e = 2.9\%$ in the GENE simulations. This latter consideration indicates that the local physical parameters of this JET pulse at $\rho_{tor} = 0.15$ sit in the region of the phase space where the KBM is linearly destabilized.

It should be noted that the large-scale branch of unstable KBMs in Figure 2 has a fluid-type nature, since the frequency of the unstable eigenmodes is comparable to the growth rate, especially for the very low wavenumber range. On the other hand, the KBM branch appearing at larger k_y has much higher frequencies but also lower growth rates, and therefore it is not expected to play an important role in the nonlinear phase.

In addition, the effects of the fast ions on the linear stability have been analysed and the outcomes are displayed in Figure 2 for the case with $R/L_{T_i} = 1.62$. The suprathermal ions have an additional destabilizing effect for the lowest binormal wavenumbers, as could be seen by inspecting the growth rate spectrum represented by the red dashed curve with filled red squares. This is likely due to the increase of the free energy destabilizing the low-k_y modes. It is important to note that the nature of the mode is not modified, as the KBMs still dominate the linear spectrum. The fast ion distribution is approximated as a Maxwellian, and the local values of density and temperature, as well as their radial gradients, are calculated starting from the integrated modelling computation. It should be however stressed that the computations of the fast-ion distribution function are affected by large uncertainties, and therefore for their assessment a more accurate scan on the fast-ion parameters is required. This is, nonetheless, out of the scope of the present work. Similar results are also obtained for the other R/L_{T_i} cases, but here not shown for the sake

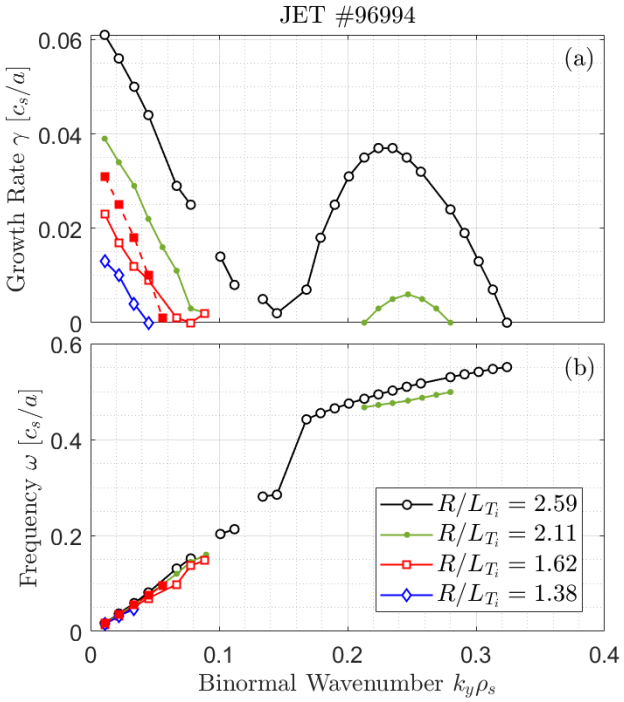

Figure 2: Growth rate (a) and frequency (b) spectra of the JET pulse #96994 at $\rho_{tor} = 0.15$ with $q = 1.05$ and $\hat{s} = 0.1$ for different values of the normalized ion temperature gradient R/L_{T_i}. The impact of the fast ions is also displayed for the case with $R/L_{T_i} = 1.62$ in dashed with red filled squares.

of simplicity.

Introducing the parallel flow shear γ_{pfs} in the simulations leads to negligible effects on the growth rate and frequency of the dominant modes. This latter parameter γ_{pfs} is obtained from the integrated modelling computation as well. In this specific case, it is computed to be low, i.e. $\gamma_{pfs} = 0.005\ c_s/a$, which is less than the KBM growth rate, and therefore its influence on the system stability is expected be low.

In Figure 4, the dependency of the KBM on $\hat{s}$ and q is displayed, showing that an important ingredient for the destabilization of the mode is the low magnetic shear. For the sake of clarity, the scan on $\hat{s}$ has been performed by keeping q constant, and vice-versa. For the scan on $\hat{s}$, $q = 1.05$, and for the scan on q, $\hat{s} = 0.1$. Figure 4 displays the results for the wavenumbers $k_y\rho_s = 0.022$ and 0.224, highlighting that the two KBM branches have similar dependencies. Furthermore, the lower the magnetic shear, the more elongated is the KBM structure along the field line in such conditions, leading therefore to narrower structures in the radial direction [28].

These latter considerations could indicate that, if any effect on the electron distribution function occurs, the magnetic shear plays an important role in determining the width of the domain affected by the unstable KBMs. Interestingly, in order to observe unstable KBMs, the magnetic shear is necessarily low.

On the other hand, the q-profile is less crucial as KBMs are also destabilized at very low q values. Therefore, in order to observe any possible effect of the KBM on the electron distribution function in such simulations, a magnetic equilibrium having $\hat{s} = 0.1$ and $q = 1.05$ has been employed in the following linear and nonlinear numerical analyses. The large uncertainty in the computation of the magnetic equilibrium in the inner plasma core justifies the possibility of adopting these deep-core values of q and $\hat{s}$. Moreover, using a sufficiently high value for the magnetic shear reduces the computational demands of the simulations.

3.3 KBM impact on the electron distribution in the linear phase

After having elucidated the nature of the instability arising in such a plasma configuration, it is important to determine the impact of such instabilities on the electron distribution function in the linear phase of the system. In panel (a) of Figure 5, the linear perturbed electron distribution δf_e is shown for the wavenumber $k_y\rho_s = 0.022$, dominated by the KBM instability, in momentum space. The momentum coordinates $p_\parallel$ and $p_\perp$ are defined consistently with the momentum defined in Section 2. In this case, the perturbation of the distribution function from the Maxwellian distribution is plotted after being averaged over the parallel direction z and summed over the connected radial modes k_x, which is equivalent to a flux-surface average in flux-tube geometry. For visualization purposes, δf_e is normalized to be within [-1,1]; the Maxwellian

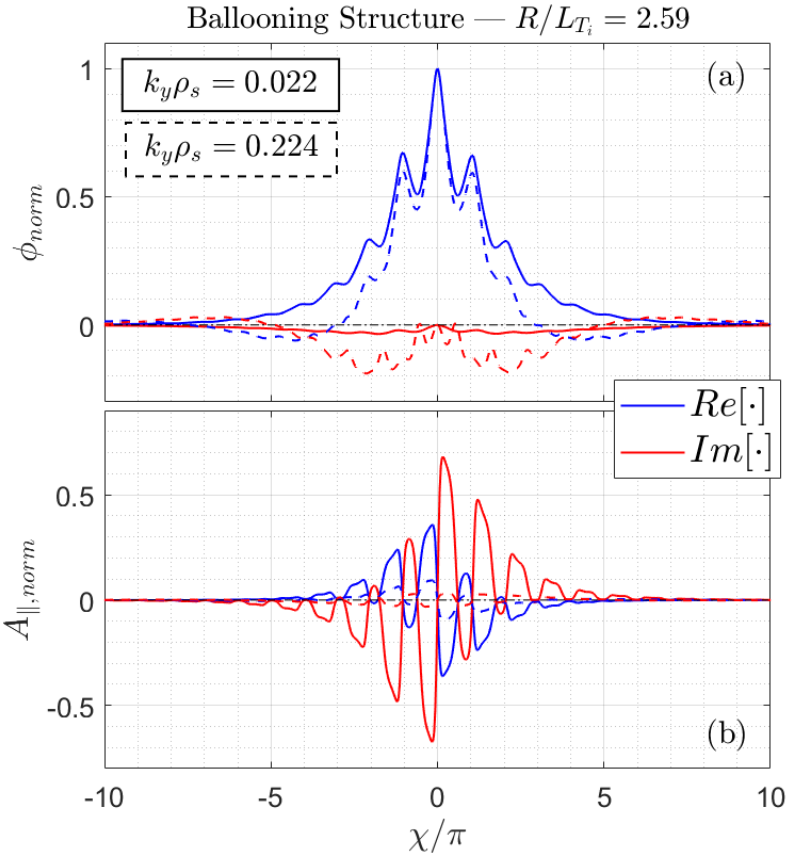

Figure 3: Normalized ballooning envelope of the electrostatic potential ϕ (a) and the magnetic potential $A_\parallel$ (b) along the ballooning angle χ. The real (blue curves) and the imaginary (red curves) components of these structures are computed through GENE linear simulations with $R/L_{T_i} = 2.59$ for $k_y\rho_s = 0.022$ (solid lines) and $k_y\rho_s = 0.224$ (dashed lines). The magnetic potential is normalized to the same factor of the electrostatic potential.

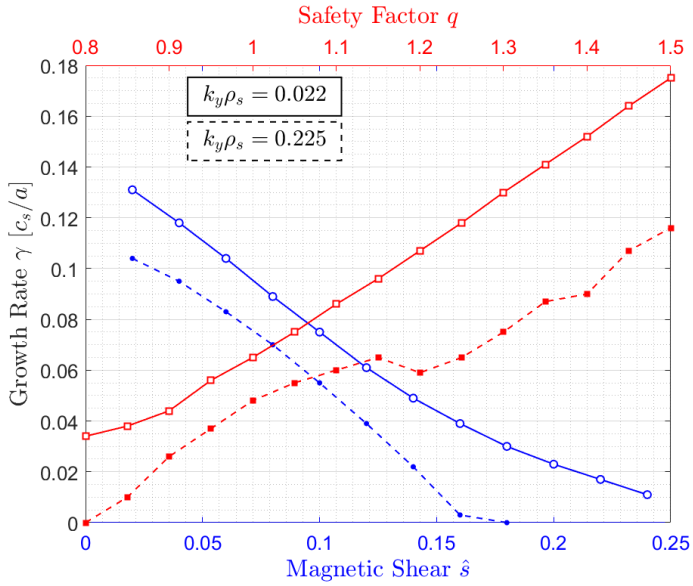

Figure 4: Linear scan over the local values of the magnetic shear (blue curves) and the safety factor (red curves) for $k_y\rho_s = 0.022$ (solid curves) and 0.224 (dashed curves) for the case with $R/L_{T_i} = 2.59$. For the scan on $\hat{s}$, $q = 1.05$, and for the scan on q, $\hat{s} = 0.1$.

$F_{M,eq}$, consistent with the parameters of the JET pulse #96994 reported in Table 1, is also normalized to be within the same domain [-1,1], and then is subtracted from δf_e. In this fashion, the plot clearly shows

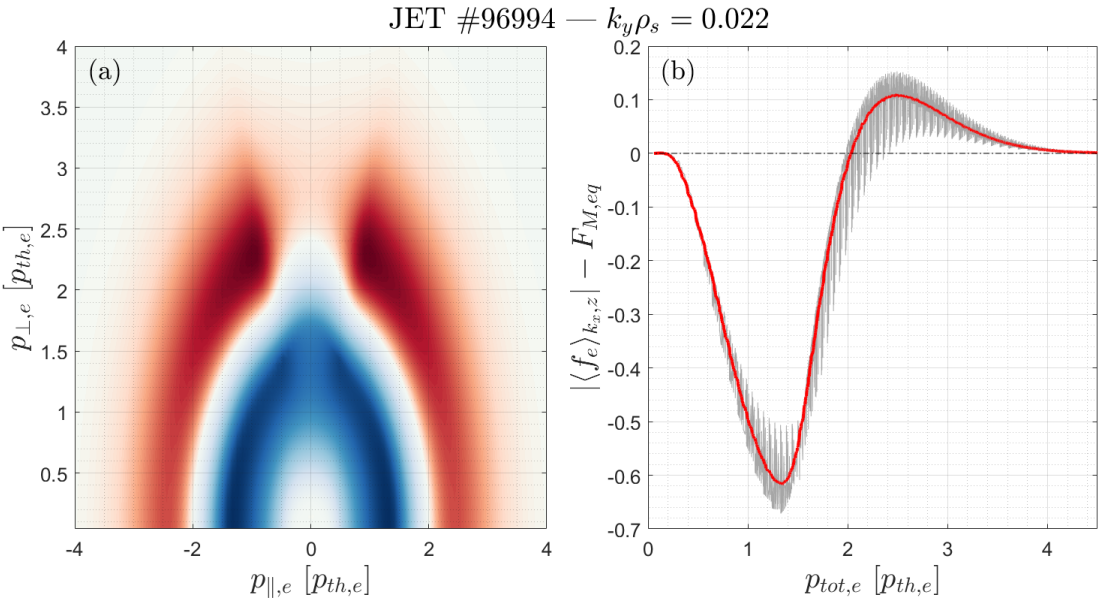

Figure 5: In (a) the electron distribution function summed over the radial modes for $k_y\rho_s = 0.022$ and averaged over the parallel direction is subtracted by an equivalent Maxwellian and then it is displayed in the momentum p space. Both distribution functions, before the subtraction, are normalized to be within the domain $[-1, 1]$. In (b), the normalized distribution function of panel (a) is integrated along the iso-momentum curves and is displayed as a function of the total electron momentum. The superposed red curve is the moving average of the integrated curve. The simulation here considered refers to the case with $R/L_{T_i} = 2.59$ without including fast ions and flow shear.

the non-Maxwellian feature of the perturbed distribution function in response to the KBM instability. As it appears clearly in Figure 5(a), the electron distribution assumes a bipolar signature in the velocity space (panel (a)). Thus, for straight comparison to the perturbation introduced in the heuristic model of Section 2, the modified perturbed distribution function of the electrons is integrated along the iso-momentum curves and then plotted as a function of the total electron momentum $p_{tot,e}$ in panel (b) of Figure 5. In such a way, the bipolar structures is even clearer, and it resembles to the perturbation shape assumed in the heuristic model of Section 2.

Figure 5 displays the linear response only for one particular binormal wavenumber, that is $k_y\rho_s = 0.022$. Nevertheless, the same kind of bipolar structure in the momentum space is observed for all the wavenumbers dominated by the KBM instability of the linear spectrum. This suggests that the KBM is responsible for such a linear perturbation of the electron distribution function.

In order to further check whether other subdominant microinstabilities are not visible through the initial value calculations, the GENE code has been employed in its eigenvalue solver version [33]. It is found that for $k_y\rho_s < 0.25$ of the linear spectra, the KBMs are the only unstable modes. This corroborates the fact that the bipolar signature in the velocity space is a clear effect of the KBMs.

3.4 Analysis of the linear perturbation causes

Interestingly, the bipolar structures in the velocity space of the KBM-dominated wavenumbers have been observed also in numerical flux-tube simulations employing an innovative moment-based approach [34] (see Figure 12 of Ref. [34]). Those numerical analyses have been performed with different input parameters with respect to the study case of this work, in particular with slightly modified radial gradients of the Cyclone Base Case [35]. This corroborates even further the identification of the KBM as the cause of such a bipolar perturbation in the velocity space, and it suggests that a generalized KBM effect on the electron distribution can be drawn.

In order to understand the origin of the bipolar perturbation, the electron diamagnetic drift frequency:

$$\omega_e^* = \left[R/L_{n_e} + R/L_{T_e}\left(p_\parallel^2 + p_\perp^2 - \frac{3}{2}\right)\right]\frac{T_e k_y}{eB_0 a} \tag{2}$$

expressed through consistent normalization with the GENE-computed quantities, is over-plotted to the real

part of the electron perturbed distribution function evaluated for $(k_x, k_y) = (0, 0.011)$ at the outboard mid-plane ($z = 0$) in Figure 6. In these simulations, for the sake of simplicity, the $\hat{s} - \alpha$ geometry is employed and the ratio T_i/T_e is assumed to be 1.

It can be clearly seen that the dashed contour lines of ω_e^* have very similar shapes with respect to the structures of the electron perturbed distribution function. The pink solid contour lines represents $\omega_e^* = \omega_{KBM}$, with ω_{KBM} the GENE-computed value of the KBM frequency for the considered binormal wavenumber. These curves are very close to the region of the momentum space where δf_e presents a negative bump, indicating that such a bump is related to the electron diamagnetic drift frequency ω_e^*. The observed discrepancy with the analytical formula may be related to some effects such as the collisions. In the figure, the region of δf_e where the bump is observed, corresponding to an arbitrary 95% of the peak, is highlighted with gold dotted contour lines. In addition, again for visualization purposes, the green dotted curve represents the exact position of $\mathrm{Re}[\delta f_e] = 0$. Along this curve, hence, the initial electron distribution function is not perturbed. It is clear that these green curves coincide almost perfectly with the contour lines of $\omega_e^* = 0$ for the various cases with combinations of R/L_n and R/L_{T_e}. The same analysis yields very similar results also

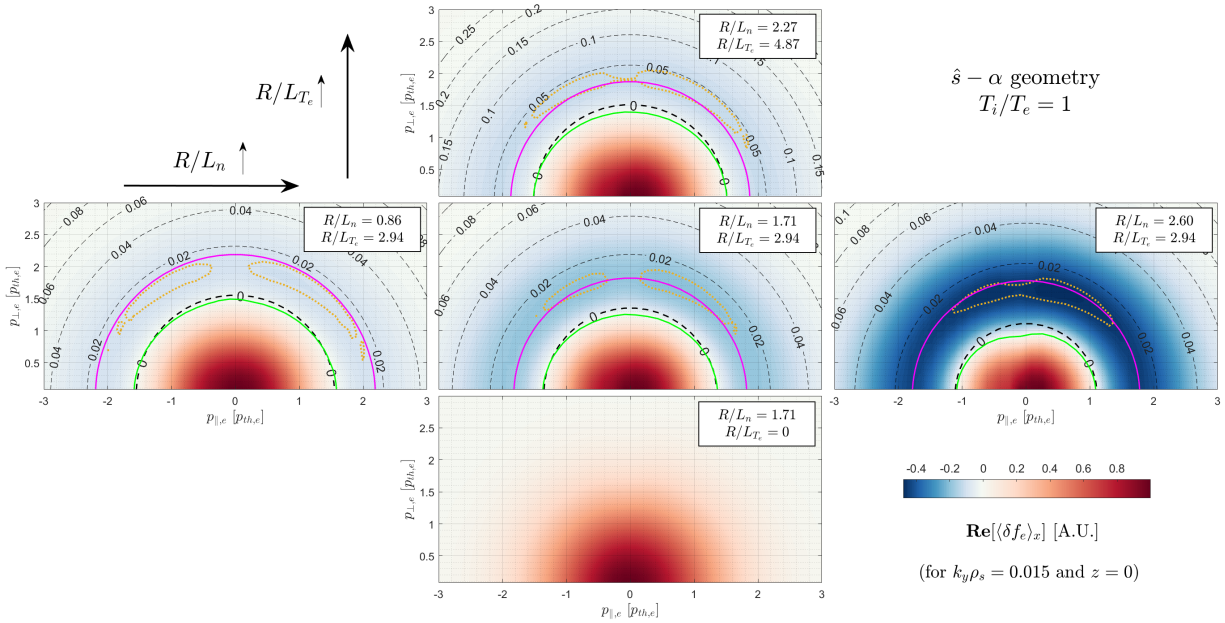

Figure 6: The real part of the perturbed electron distribution function $\mathbf{Re}[\delta f_e]$, for $k_y\rho_s = 0.011$ and $k_x\rho_s = 0$ is displayed in the momentum space for different combinations of R/L_n and R/L_{T_e}. These simulations have been performed in $\hat{s} - \alpha$ geometry with $T_i/T_e = 1$. The dashed contour lines represent the electron diamagnetic drift frequency ω_e^* (normalized to c_s/a), with the frequencies corresponding to 0 and to the KBM frequency highlighted respectively with wider dashed black and solid pink curves. In addition, the green solid curves represent the position at which $\mathbf{Re}[\delta f_e] = 0$, while the gold dotted curves represent the region where the negative peak of $\mathbf{Re}[\delta f_e]$ is found (the 95^{th} percentile of such a minimum). In the panel at the bottom, no contour lines are over-plotted because with $R/L_{T_e} = 0$, ω_e^* loses its dependence on the velocity space.

for other binormal wavenumbers dominated by the KBM instability in the linear spectra reported in Figure 2. Moreover, analyzing parallel positions different from the outboard mid-plane does not change the results of the analysis.

To further corroborate the observation of the strict link between δf_e and ω_e^*, the effects of the local density and temperature gradient on the bipolar structure position in the momentum space is analyzed. This is because in Equation 2 the two main parameters regulating ω_e^* are essentially R/L_{n_e} and R/L_{T_e}. Therefore, it is expected that, if any interaction takes place, the structures would move accordingly to the modification of the electron diamagnetic drift frequency. In particular, Equation 2 has the analytical form of a circumference, with the radius

$$r_{pos} = \sqrt{\frac{\omega_e^*}{R/L_{T_e}} \cdot \frac{eB_0 a}{T_e k_y} + \frac{3}{2} - \frac{R/L_{n_e}}{R/L_{T_e}}} \tag{3}$$

This radius can thereby be related to the position of the structures in the momentum space. In Figure 6, the results of numerical analysis with different R/L_{n_e} and R/L_{T_e} for the binormal wavenumber $k_y\rho_s = 0.011$

and $k_x = 0$ are also displayed. Furthermore, the peaking of the KBM unstable modes at $k_x = 0$ justifies the choice of such radial wavenumber to be displayed.

As expected, when the normalized electron density gradient is decreased, the position of the structure of δf_e in the momentum space is localized at higher energies. On the opposite direction, when the normalized electron temperature gradient is decreased, the dependence of ω_e^* on the momentum space weakens and the resonant structures tend, thereby, to shrink and disappear. Indeed, in the bottom panel of Figure 6, the case with $R/L_{T_e} = 0$ is displayed, and no contour lines are over-plotted because for such a value ω_e^* loses its momentum space dependence. As a matter of fact, in such a panel, the δf_e is almost perfectly a Maxwellian, and no perturbations are found. Therefore, this picture is further demonstrating that a clear interaction between the electron diamagnetic drift motion and the KBM instability is occurring, generating thus the bipolar signature in the velocity phase space of the electron distribution function.

It is further suggested that a small change in the local pressure gradient of the electrons may move the characteristic bipolar structures in a different position in momentum space. Indeed, the local pressure gradient in the plasma core can vary because of different heating systems, power deposition profiles or local magnetic equilibrium parameters. Therefore, the great variance of the position and the width of the bipolar structure, which is adopted in the heuristic model and is necessary to match the outcomes from different JET plasma scenarios, is consistent with such a strong dependence of the KBM-driven bipolar structures on the local parameters R/L_{n_e} and R/L_{T_e}.

Eventually, the same kind of analysis displayed in Figure 6 is also performed for the more realistic input parameters of JET pulse #96994 at $\rho_{tor} = 0.15$ with the Miller magnetic geometry. The outcomes of this additional analyses are shown in Figure 7. It appears that also in this specific case, a remarkable

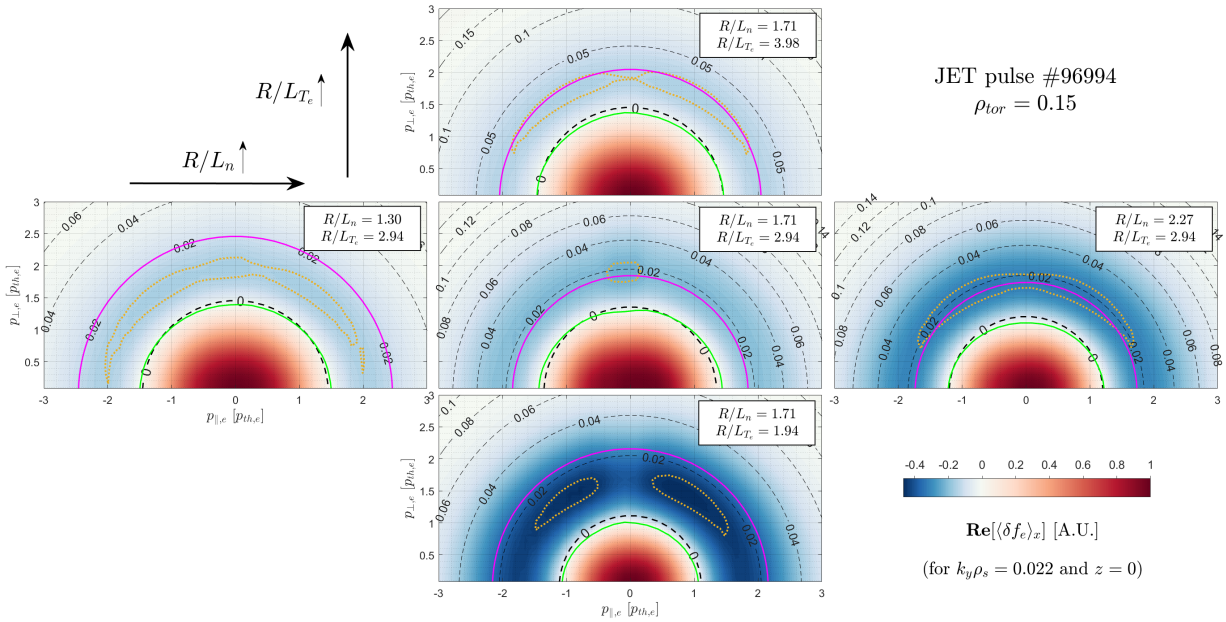

Figure 7: The real part of the perturbed electron distribution function $\mathbf{Re}[\delta f_e]$, for $k_y \rho_s = 0.022$ and averaged over the radial direction for the case with $R/L_{T_i} = 2.59$ is displayed in the momentum space for different combinations of R/L_n and R/L_{T_e}. The dashed contour lines represent the electron diamagnetic drift frequency ω_e^* (normalized to c_s/a), with the frequencies corresponding to 0 and to the KBM frequency highlighted respectively with wider dashed black and solid pink curves. In addition, the green dotted curves represent the position at which $\mathbf{Re}[\delta f_e] = 0$, while the gold dotted curves represent the region where the negative peak of $\mathbf{Re}[\delta f_e]$ is found (the 95^{th} percentile of such a minimum).

correspondence between the structures of the perturbed electron distribution function and the electron diamagnetic drift frequency is obtained when the KBM is the dominant linear instability.

Nevertheless, although a clear relation between the KBM-driven bipolar structures of δf_e and ω_e^* exists, the physical causes of such a perturbation are still elusive. This could be investigated in a future effort by analytically calculating the competition between the various drive terms in the gyrokinetic equation, similarly to what done in, e.g., [17]. Furthermore, as reported in the Appendix A of Ref. [34], the non-adiabatic contributions to the distribution function is dependent on the diamagnetic frequency (see Eqs. A2c and A3c). Hence, this may explain the correspondence of the contour line $\omega_e^* = 0$ with the contour of $\delta f_e = 0$ that has been thoroughly observed in this section. However, the causes of the correspondence between the peak of the perturbed distribution function and the contour line $\omega_e^* = \omega_{KBM}$ remains unclear. It could be

speculated that specific resonant effects are effective. Therefore this must be investigated more in detail in a future study.

3.5 KBM impact on the electron distribution in the nonlinear phase

In the linear phase of the system evolution, the amplitude of the perturbation cannot be evaluated due to the continuously growing character of the linear response. Indeed, this can only be evaluated with nonlinear simulations, where the evolution of the system may also reveal whether the signature is static in time or it is related only to a specific linear phase of the distribution function perturbation. Moreover, in the nonlinear phase, all the possible cross-scale interactions among the binormal and radial wavelengths are retained, and this may be crucial in the final evaluation.

Thus, in this section, the nonlinear evolution of the system is assessed in order to evaluate the characteristics of the KBM impact on the electron distribution function. However, it should be stressed that the purpose of this study is the analysis of the impact of the KBM on the electron distribution function in the nonlinear phase, and not the experimental validation of the GENE simulations. In this sense, we mainly discuss and consider the evolution of the momentum-space structure of the perturbed electron distribution, without evaluating the transport and its matching with the experimental outcomes. This task requires more accurate analysis, for instance including all the ingredients that could have a strong impact on the transport level, such as the suprathermal ion species and the flow shear effects. It should also be clarified that the distribution function reported in the following analyses is examined at the outboard mid-plane for $k_y = 0$.

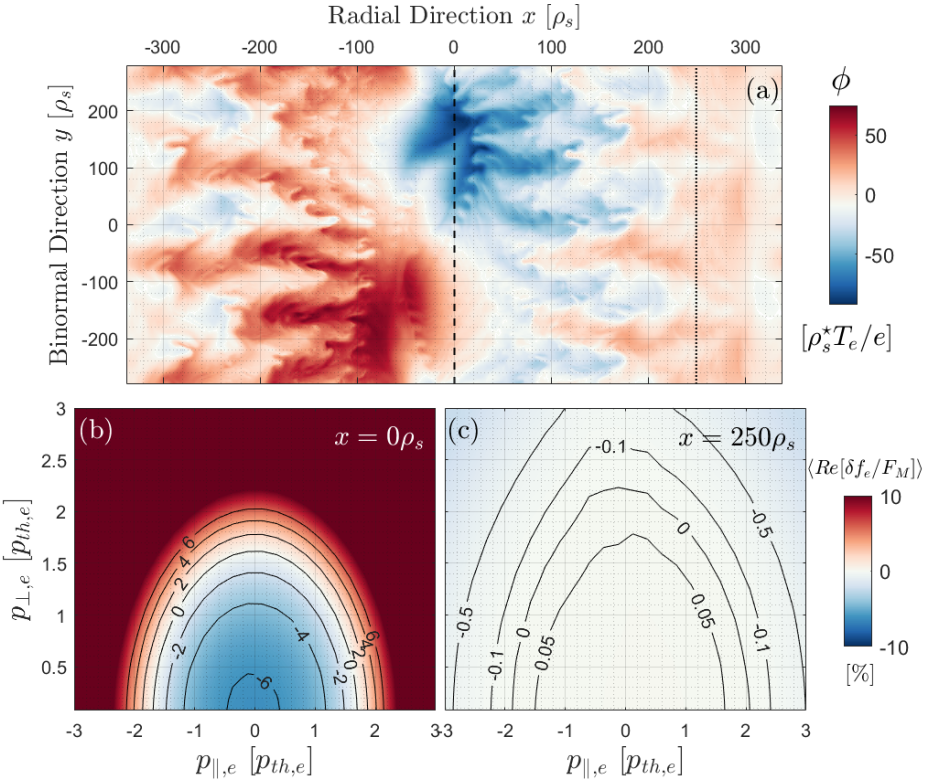

Figure 8: (a) Snapshot of the inverse-Fourier transformed electrostatic potential ϕ at the outboard mid-plane and at $t = 740$ $[a/c_s]$ for the simulations with $R/L_{T_i} = 1.62$. The vertical dashed and dotted lines refer to the positions $x = 0\rho_s$ and $x = 250\rho_s$. Panels (b) and (c) displays the time-averaged perturbed electron distribution function δf_e over the equilibrium Maxwellian F_M respectively for the same radial positions, $x = 0\rho_s$ and $x = 75.5\rho_s$. The perturbed distribution function is averaged over the binormal direction and over the time window $t = 740 \pm 50$ $[a/c_s]$, and evaluated at $z = 0$, i.e. at the outboard mid-plane.

Panels (b) and (c) of Figure 8 display the perturbed distribution for two different radial positions, which are respectively $x = 0\rho_s$ (the centre of the flux-tube) and $x = 250\rho_s$. In such plots, the electron distribution is taken at $z = 0$ and for $k_y = 0$ (which can be related to an average over the binormal direction), selected for the specific radial positions reported above, and eventually averaged over a significant time window of the nonlinear simulation. This Figure refers to the case with $R/L_{T_i} = 1.62$, which is lower than the value computed by the integrated modelling at such a radial location ($R/L_{T_i} = 2.59$). This value of ion

temperature gradient has been chosen since at higher R/L_{T_i}, the GENE-computed fluxes are unrealistically huge, and the nonlinear simulations are thereby likely unreliable. The two panels have the same colorbar, which has been restricted to the upper limit of 10% to facilitate the visualization. The two selected radial positions are representative of two differently characterized regions of the perpendicular domain. Indeed, $x = 0\rho_s$ is in the middle of a turbulent structure driven by the KBM and moving mostly along the binormal direction; on the other hand, $x = 250\rho_s$ represents a region with a much lower turbulent activity. These considerations are illustrated by panel (a) of Figure 8, where a snapshot in time of the electrostatic potential ϕ is shown in the perpendicular (x, y) domain for the parallel position $z = 0$. For the sake of clarity, in the electrostatic potential contour, all the (k_x, k_y) modes have been retained. The time snapshot is chosen to fall within the time window of interest for the time-average done on the electron distribution functions of panels (b) and (c). It could be seen, thus, that the electron distribution is strongly modified with respect to an equivalent Maxwellian in the region where the radially localized KBM is located, whereas it is almost not affected for $x = 250\rho_s$. The contour lines for panel (c), indeed, show that in the momentum space a very tiny discrepancy with the initial Maxwellian distribution is found. Moreover, the same kind of bipolar structure is observed for panel (b), aligned with the shape of the linear perturbation reported in Figure 5. This confirms that the bipolar perturbation is essentially due to the radially localized KBM instability arising in these plasma conditions.

Furthermore, the large ratio $\langle|\delta f_e/F_M|\rangle_{y,t}$ occurring in extended momentum regions is due to the fact that those regions correspond to the tail of the Maxwellian distribution. Hence, a very small deviation from it could lead to a strong difference in percentage.

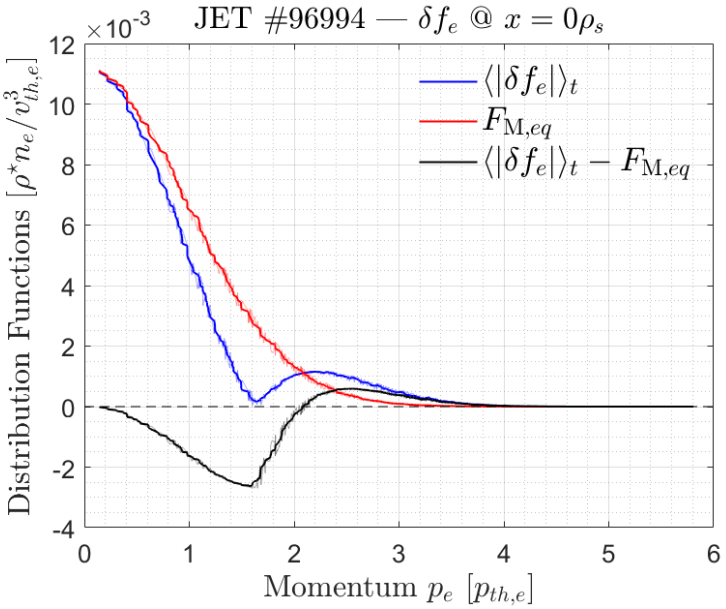

Figure 9: The blue and red curves represent, respectively, the absolute value of the perturbed electron distribution function averaged in time and along the binormal direction for the specific radial position at the center of the flux tube ($x = 0\rho_s$) and the equivalent Maxwellian $F_{\mathrm{M},eqs}$ rescaled to have the same maximum values of $\langle|\delta f_e|\rangle_t$ as a function of the total momentum p. The isolated perturbation, i.e. the perturbed distribution function subtracted by the rescaled Maxwellian, is displayed in black.

If the distribution function of Figure 8(b) is displayed as a function of the total momentum, as done in Section 3.3, a one-dimensional curve can be obtained and compared to the perturbation assumed in the heuristic model. The thus obtained modified nonlinear electron distribution function averaged in time is shown in Figure 9, where the absolute value of the perturbed distribution function is subtracted by a rescaled equivalent Maxwellian $F_{M,eq}$. The Maxwellian is rescaled such that the maximum of the Maxwellian matches the maximum of the perturbed distribution function. Once more, this is done to highlight the non-Maxellian part of the distribution function which is the one affecting the ECE measurement. It should be also noted that the position of the center of the bipolar perturbation in momentum space in such nonlinear simulation is very similar to the one measured in the corresponding linear simulation for the dominant binormal wavenumber of the spectrum (i.e. $k_y\rho_s = 0.011$).

More studies have been carried out recently to characterize different microinstability-induced perturbations in velocity space [34], and the nature such a structure observed for instance in Figure 5(a) has not been identified. As an example, the same kind of analysis has been carried out for the standard Waltz GA

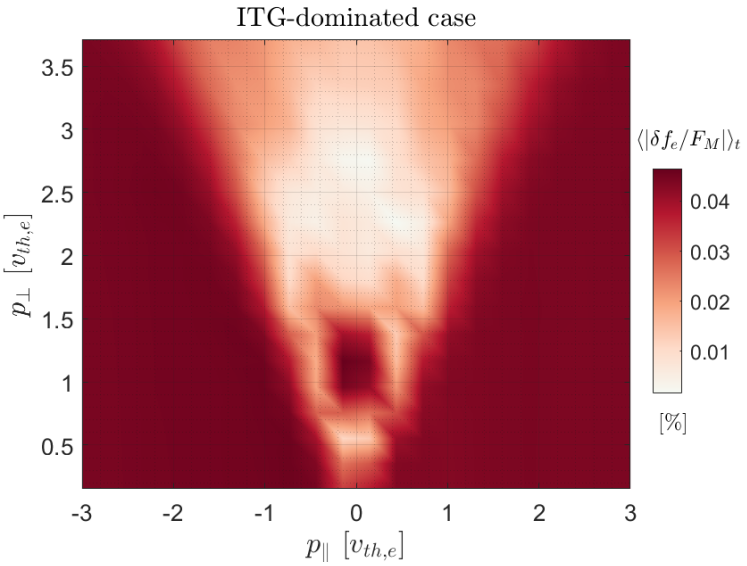

Figure 10: Time-averaged absolute value of the perturbed electron distribution function δf_e over an equivalent Maxwellian F_M for the ITG-dominated Waltz standard case. The perturbed distribution function is considered at the outboard mid-plane.

case [36], which is dominated by the Ion Temperature Gradient (ITG) instability [37] at the ion-scale. In such a case, the shape of the perturbation is totally different from that observed for instance in Figures 5(a) and 8(b). For the sake of clarity, the perturbed electron distribution function over an equivalent Maxwellian in the ITG-dominated case is reported in Figure 10. Moreover, the amplitude of the perturbation is more than two orders of magnitude lower with respect to the KBM-dominated case.

Although the consideration of uniqueness would require more extensive analyses, it could be concluded that this perturbation in the momentum space is not systematically observed but it is characteristic of specific radially localized instabilities such as the KBMs.

3.6 Effects of the KBM drive on the perturbation amplitude and position

The shape of the perturbation induced by the KBM is strongly reminiscent of the bipolar structure that has been employed in the heuristic model to retrieve the T_e measured by the ECE (see Section 2). Indeed the one employed in the model for this exact JET pulse, i.e. #96994, is $\sim$5% depending on the lobe of the perturbation. The amplitude of the perturbation depends on the strength of the KBM drive. To show this, the absolute value of the perturbed distribution function normalized to the equivalent Maxwellian and averaged in time is shown for 3 different values of R/L_{T_i} in Figure 11. The perturbation is affected by the KBM intensity, which is linked to the drive of the instability – i.e., the ion temperature gradient in this specific analysis. The same kind of bipolar structure is obtained for the different cases, but the amplitude increases with R/L_{T_i}. The contour curves help in detecting such increase of the perturbation amplitude especially in the low-momentum lobe of the bipolar structure. The three different δf_e are calculated over the time windows which are highlighted with colored bands in Figure 12. In such a figure, the time evolution of the electron and ion heat fluxes is displayed for the three different cases.

As one can observe, the fluxes of these simulations are not entirely converged (especially for the case with $R/L_{T_i} = 1.54$), although the time-dynamic seems to suggest a slow approach to low values of the fluxes. The averaged heat fluxes, especially for the ion counterpart, are larger for the higher values of R/L_{T_i}. It should be remarked, as already done previously, that the purpose of these simulations is not to determine the heat fluxes generated by the turbulence, as this would require more accurate analyses (e.g., including the fast ions, non-local and flow shear effects) for an experimental validation. The goal of this study is indeed to determine the nonlinear evolution of the bipolar structures in momentum space of the electron perturbed distribution in the presence of unstable KBMs. Indeed, in these cases, δf_e seems to be quasi-steady in the selected time windows, corroborating the secular presence of the structure in momentum space.

Moreover, in the GENE the KBM-induced fluctuations in the electron temperature are dominated by structures that are quite localized, with a radial width of $\lesssim$15 cm. Yet, multiple weak turbulent eddies are observed when higher KBM drive are considered, i.e. when the ion temperature gradient is increased. This consideration may reveal to be important when considering the width of the plasma region in which the effects

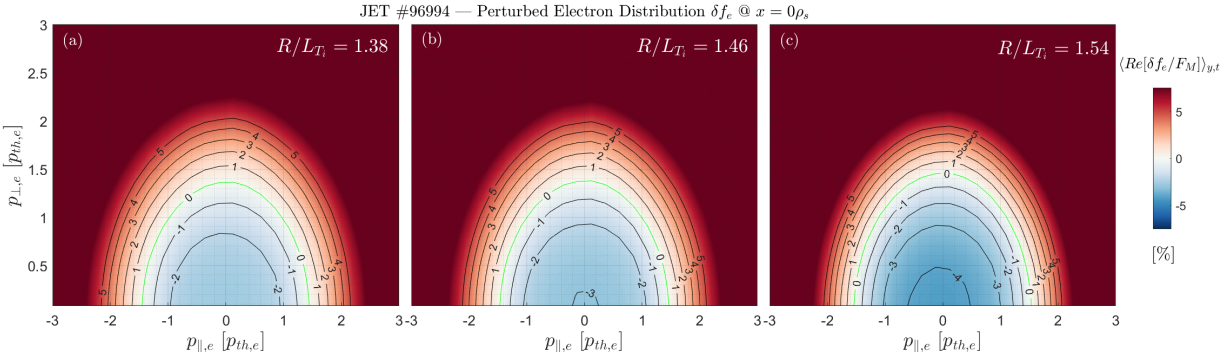

Figure 11: Time-averaged perturbed electron distribution function δf_e over an equivalent Maxwellian F_M for three different values of the normalized ion temperature gradient, which are $R/L_{T_i} = 1.38$ (a), 1.46 (b) and 1.54 (c). The perturbed distribution functions are all considered at the same radial location ($x = 0\rho_s$) and at the outboard mid-plane ($z = 0$).

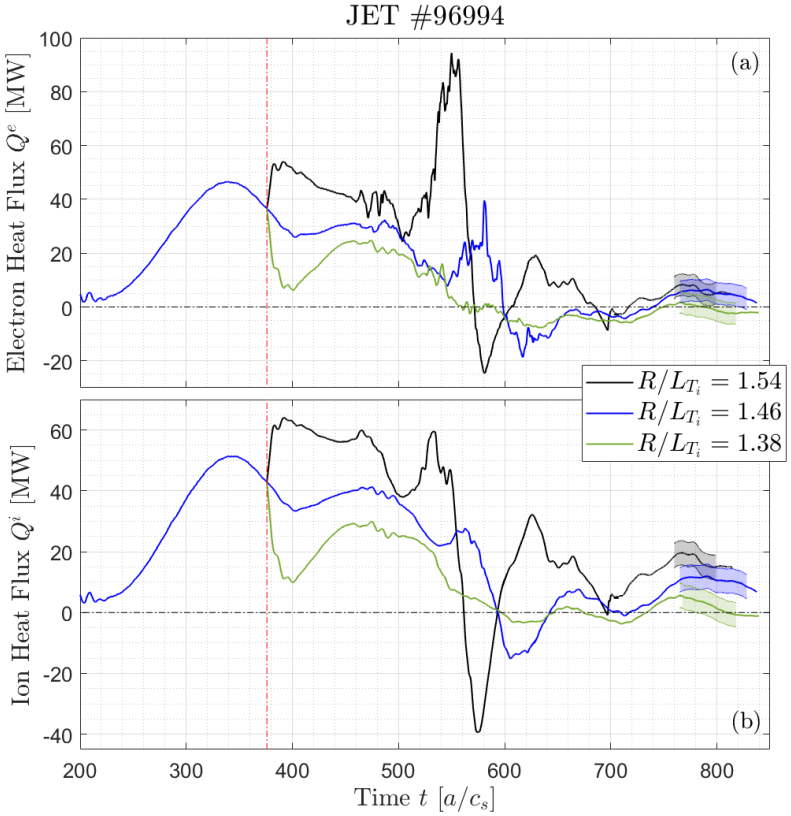

Figure 12: Total Electron (a) and Deuterium (b) heat fluxes for different values of the ion temperature R/L_{T_i} computed through nonlinear GENE simulations. The highlighted bands represent the time windows over which the time average of the perturbed electron distribution functions displayed in Figure 11. The vertical red line represents the time at which the R/L_{T_i} has been modified from the simulation with $R/L_{T_i} = 1.46$.

of the KBM on the electron distribution function are noteworthy. Although the flux-tube approximation has been employed, this results suggests that the main structures in the poloidal section of the KBM-induced fluctuations may affect a wider radius, and thereby multiple ECE diagnostic channels, depending on the KBM drive (i.e. on the local gradients as well as on the β).

Interestingly, in Figure 11 only the amplitude of the structures varies, while the position in momentum space remains almost unaltered when varying R/L_{T_i}. This is consistent with the picture discussed previously in Section 3.4. Indeed, the structure position is intimately related to the electron diamagnetic drift frequency ω_e^*, which does not depend on the ion temperature gradient. However, as observed in Section 2, the position of the bipolar structure calculated by the heuristic model to better match the ECE temperature measurements

Table 2: Modified plasma parameters considered in further GENE simulations to achieve better position matching between the bipolar structures imposed in the heuristic model and obtained in the gyrokinetic modelling.

	$\hat{s}$	R/L_n	R/L_{T_e}	R/L_{T_i}
Case 1	0.15	2.92	2.80	0.16
Case 2	0.15	2.59	2.59	0.32

for this JET pulse #96994 is centered around $p_e = 1.1\ p_{th,e}$. There is, hence, a slight difference with respect to that computed in these GENE simulations, which is always centered at larger momentum regions.

Therefore, following the recipe displayed in Figure 7, the options to displace the center of the bipolar structure at lower momentum values are either to increase the density gradient R/L_n or to decrease the electron temperature gradient R/L_{T_e}. Nevertheless, the KBM drive is strongly increased by increasing the R/L_n, leading to an abrupt rise of the turbulent fluxes similarly to a non-zonal transition [38, 39], and thereby impairing the soundness of the simulations. On the other hand, by decreasing the electron temperature gradient, also the KBM drive is decreased. This leads to a Dimits-shift-like regime [35, 40] in which the KBM are marginally stable linearly but stable nonlinearly. Hence, this latter option is not suitable, since the KBM must be found nonlinearly unstable to affect the electron distribution. For these reasons, we have decided to increase the magnetic shear and consequently decrease the linear growth rate of the KBMs, as shown in Figure 4. Indeed, by increasing $\hat{s}$, at a fixed value of q, the KBMs tend to be stabilized. This allows for a better flexibility in adjusting the drive of the instability, and in particular to increase the R/L_n, without causing an abrupt and unrealistic rise of the turbulent fluxes. Yet, the parameter space remains narrow, making the task complicated.

Thus, two new plasma configurations have been designed with larger magnetic shear and R/L_n, and with slightly lower R/L_{T_e}. For the ion counterpart, the temperature gradient has been strongly reduced, in order to further decrease the KBM drive and only allow for weak marginal destabilization of the KBM in the nonlinear phase. This tailoring of the local input parameters of the flux-tube simulations, summarized in Table 2, is again justified by the large uncertainties in the experimental evaluation of the plasma parameters in the deep core region.

The main outcomes of these further simulations are displayed in Figure 13, in which the electron perturbed distribution function is displayed. The labelling *Case 1* and *Case 2* follows the indication given in Table 2. As expected, the point at which the time-averaged bipolar perturbation in the electron distribution function

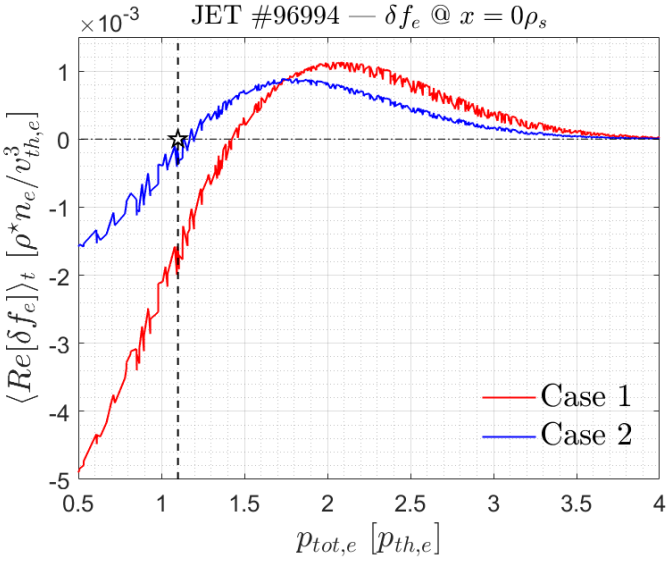

Figure 13: Time-averaged real part of the perturbed electron distribution function δf_e as a function of the electron momentum $p_{tot,e}$ for two further simulations with increased magnetic shear. The perturbed distribution functions are considered at the same radial location ($x = 0\rho_s$) and at the outboard mid-plane ($z = 0$). The black star and the vertical dashed black curve indicate the position of the perturbation introduced in the heuristic model of Section 2 that better fits the experimental ECE measurements.

crosses the zero value occurs at smaller momentum regions. This point could be intended as the center of the

perfectly sinusoidal perturbation purposely introduced in the heuristic model of Section 2. For the *Case 2* configuration (the blue curve of Figure 13), such point of the perturbed distribution function is remarkably close to the center of the imposed perturbation of the heuristic model (black star in the figure). Despite a non-negligible difference (∼1% vs. ∼5%), the amplitude of the bipolar perturbation for this configuration is still comparable to the one introduced in the heuristic model.

It should be, however, highlighted that the heat fluxes of the two further simulations still present very high level of KBM-induced turbulent transport. For *Case 1*, an abrupt rise of the electromagnetic component of the electron flux is observed, followed by a strong increase also of the electrostatic fluxes. This leads to unrealistic levels of radial outward turbulent transport (more than two orders of magnitude larger than the power balances). For *Case 2* on the other hand, the fluxes remain under a reasonable level, although still very large with respect to the experimental power balances (aroiund 10 times larger). Again, we should stress that the purpose of those simulations is not to match the experimentally-inferred fluxes, but rather to determine the impact of the KBM instability on the electron perturbed distribution function in order to address a possible cause for the long-standing ECE-TS discrepancy problem [3–5].

In conclusion, the further plasma parameter configurations designed to better match the perturbation introduced in the heuristic model for this particular JET pulse #96994 followed the expected scaling of the electron diamagnetic frequency, as described in Section 3.4. The delicate balance between the sufficiently large drive to nonlinearly destabilize the KBMs and the very huge turbulent fluxes is challenging to be found. Many input parameters may be fine-tuned to find the optimum spot in the parameter phase space to both match the experimental power balance and the amplitude and position of the KBM-induced bipolar structure. Yet, this experimental validation would require a even bigger amount of computational resources, which is out of the scope of this work.

4 Conclusions

Flux-tube gyrokinetic numerical analyses of the deep core plasma of the JET high-performance pulse #96994 have been performed in order to investigate the possible cause of the long-standing issue of the ECE-TS discrepancy observed for decades in the core region of high temperature plasmas [3–5]. Indeed, a recent database of high-performance pulses built for the latest JET campaigns [11] has renewed this puzzling issue. Thus, an heuristic model introducing a localized perturbation in the momentum phase space of the electron distribution function is capable to reconcile the experimental discrepancy [12, 14]. Yet, the causes of such perturbation are still elusive.

In this study, the KBM instability, destabilized in the core of high-performance and high-β plasmas, is proposed as a possible cause of the perturbation in the electron distribution. The simulations performed with the flux-tube version of the GENE code highlight that the perturbed electron distribution function is affected by the unstable KBM. The generation of a bipolar structure similar to the one assumed in the heuristic model is observed in the momentum space of δf_e in such linear simulations. Additional analyses corroborate this effect by showing that the position of the bipolar structure in momentum space follows the electron diamagnetic frequency $\omega_e^\star$. At this regard, it is observed that there is a correlation between the position at which the perturbed electron distribution function goes to zero and the position of $\omega_e^* = 0$ in momentum space. This position fulfils the relation

$$p_0 = \sqrt{\frac{3}{2} - \frac{R/L_{n_e}}{R/L_{T_e}}} \tag{4}$$

as it follows from Equation 3 by setting $\omega_e^* = 0$. This particular radius is linked to the central position p_0 of the perturbation in momentum space of the heuristic model, and could give interesting insights for further experimental studies.

The nonlinear simulations corroborate even further these findings, demonstrating that such a bipolar perturbation arises at the destabilization of the KBM and remains all along the simulated time. Furthermore, it is reported that the strength of the perturbation observed in these nonlinear simulations is related to the amplitude of the KBM-induced turbulence, which is in turn correlated with the KBM drive. On the other hand, as already found in linear computation, the position of the bipolar structure is linked to the plasma parameters determining the electron diamagnetic frequency, i.e. the local electron temperature and density gradients.

This latter consideration is coherent with the large variability of the perturbation positions used in the heuristic models to achieve good matching with different plasma conditions and scenarios in the analyzed JET pulse database. As a matter of fact, a small change of the local pressure gradient determines a substantial change in the electron diamagnetic frequency and, thereby, in the KBM-induced bipolar structure in momentum space. This small changes may be due, for instance, to the different auxiliary heating systems

employed in the different scenarios. It is, indeed, well-known that the fast ions generated through NBI or ICRH have different impacts on the electron radial profile evolution.

Further analyses revealed also that the KBM-induced electron temperature fluctuations are represented by mainly poloidally oriented eddies with a limited radial width of $\lesssim$15 cm. However, the radial region affected by the KBM-induced turbulent eddies depends on the KBM drive. It should be mentioned here that for a more precise evaluation, global simulations must be performed.

The result of this study, thus, indicates that the KBM destabilized in the deep core of high-temperature plasmas may explain the ECE-TS measurement discrepancy. The KBM-induced perturbation in the electron distribution function has been shown to be comparable in both position and amplitude with respect to the one employed in the heuristic model. Yet, some differences are still to be explained, such as the asymmetry of the lobes of the bipolar structure observed in GENE simulations. Moreover, large uncertainties in the plasma parameters of this deep core region may affect the quality of the experimental validation. Indeed, KBM drives such as the ion and electron temperature gradients, the density gradients and β, as well as the magnetic equilibrium parameters are not known with enough accuracy in this plasma regions and a fine-tuning of the inputs of the gyrokinetic modelling is expected to be challenging. Wider scans of the basic input parameters are required for a more accurate match between the two model outputs. Moreover, the inclusion of additional ion species, among which the fast ions, may play an important role is retained to be of paramount importance in addressing the experimental validation of such simulations.

Eventually, the GENE model assumes as an initial distribution a Maxwellian function for all the species. Nevertheless, preliminary results from recent studies with an improved Fokker-Planck modelling indicate that the collisional relaxation of the suprathermal particles on the electron distribution function may lead to perturbations in the energy space displaying a non-Maxwellian character [15]. It should be also stated that such a perturbation of the electron distribution function is small compared to the one assumed in the heuristic model [14] discussed in Section 2. However, there is the possibility that the two mechanisms, i.e. the collisional relaxation of the fast particles and the impact of radially localized instabilities on the electron distribution, may be present at once and therefore have a combined effect. In addition to this, other possible causes linked to the presence of low-frequency MHD modes in the plasma core have also been investigated [41].

Acknowledgements

The authors acknowledge Philipp Lauber for illuminating discussions about the fundamental idea behind this work, and Justin Ball and Moritz Pueschel for very useful discussion on the numerical simulations.

The simulations were performed on Marconi HPC system in the framework of the projects FUA37_WPJET1, FUA38_WPTEmo24 and partly on CSCS Piz Daint HPC system in the project s1097.

This work has been carried out within the framework of the EUROfusion Consortium, funded by the European Union via the Euratom Research and Training Programme (Grant Agreement No 101052200 — EUROfusion). Views and opinions expressed are however those of the author(s) only and do not necessarily reflect those of the European Union or the European Commission. Neither the European Union nor the European Commission can be held responsible for them.

References

[1] A. E. Costley, R. J. Hastie, J. W. M. Paul, and J. Chamberlain. Electron cyclotron emission from a tokamak plasma: experiment and theory. *Physical Review Letters*, 33(13):758, 1974.

[2] J. Sheffield, D. Froula, S. H. Glenzer, and Neville C. Luhmann Jr. *Plasma scattering of electromagnetic radiation: theory and measurement techniques*. Academic press, 2010.

[3] I. Fidone, G. Giruzzi, and G. Taylor. Plasma diagnostics in the tokamak fusion test reactor using emission of electron cyclotron radiation at arbitrary frequencies. *Physics of Plasmas*, 3(6):2331–2336, 1996.

[4] G. Taylor and R. W. Harvey. Assessment of an oblique ECE diagnostic for ITER. *Fusion Science and Technology*, 55(1):64–75, 2009.

[5] E. De La Luna, V. Krivenski, G. Giruzzi, C. Gowers, R. Prentice, J. M. Travere, and M. Zerbini. Impact of bulk non-maxwellian electrons on electron temperature measurements. *Review of Scientific Instruments*, 74(3):1414–1420, 2003.

[6] V. Krivenski. Electron cyclotron emission by non-maxwellian bulk distribution functions. *Fusion Engineering and Design*, 53(1-4):23–33, 2001.

[7] G. Giruzzi. Electron cyclotron emission during electron cyclotron heating in tokamaks. *Nuclear Fusion*, 28(8):1413, 1988.

[8] S. L. Prunty. A primer on the theory of thomson scattering for high-temperature fusion plasmas. *Physica Scripta*, 89(12):128001, 2014.

[9] K. V. Beausang, S. L. Prunty, R. Scannell, M. N. Beurskens, M. J. Walsh, E. de La Luna, and JET EFDA Contributors. Detecting non-maxwellian electron velocity distributions at JET by high resolution thomson scattering. *Review of Scientific Instruments*, 82(3), 2011.

[10] A. E. White, A. E. Hubbard, J. W. Hughes, P. T. Bonoli, M. E. Austin, A. Bader, R. W. Harvey, Y. Lin, Y. Ma, M. L. Reinke, et al. Investigation of the thomson scattering-ece discrepancy in ICRF heated plasmas at alcator C-Mod. *Nuclear Fusion*, 52(6):063021, 2012.

[11] M. Fontana, G. Giruzzi, F. P. Orsitto, E. de la Luna, R. Dumont, L. Figini, D. Kos, M. Maslov, S. Schmuck, C. Sozzi, et al. Investigation of T_e measurements discrepancies between ECE and Thomson diagnostics in high-performance plasmas in JET. In *EPJ Web of Conferences*, volume 277, page 03006. EDP Sciences, 2023.

[12] M. Fontana, G. Giruzzi, F. P. Orsitto, E. de la Luna, R. Dumont, L. Figini, D. Kos, M. Maslov, S. Schmuck, L. Senni, et al. High T_e discrepancies between ECE and thomson diagnostics in high-performance JET discharges. *Physics of Plasmas*, 30(12), 2023.

[13] J. Mailloux et al. Overview of JET results for optimising ITER operation. *Nuclear Fusion*, 62(4):042026, 2022.

[14] G. Giruzzi, M. Fontana, F. P. Orsitto, E. de la Luna, R. Dumont, L. Figini, M. Maslov, S. Mazzi, S. Schmuck, L. Senni, et al. A model of non-maxwellian electron distribution function for the analysis of ECE data in JET discharges. In *EPJ Web of Conferences*, volume 277, page 03005. EDP Sciences, 2023.

[15] R. Dumont et al. *in preparation*, 2024.

[16] W. M. Tang, J. W. Connor, and R. J. Hastie. Kinetic-ballooning-mode theory in general geometry. *Nuclear Fusion*, 20(11):1439, 1980.

[17] K. Aleynikova and A. Zocco. Quantitative study of kinetic ballooning mode theory in simple geometry. *Physics of Plasmas*, 24(9), 2017.

[18] G. Giruzzi et al. Evidence of bipolar perturbations of the electron distribution function in high-performance JET plasmas. In *29th IAEA Fusion Energy Conference, London, United Kingdom, 16-21 October 2023*, 2023.

[19] J. Garcia, E. De La Luna, M. Sertoli, F. J. Casson, S. Mazzi, Ž. Štancar, G. Szepesi, D. Frigione, L. Garzotti, F. Rimini, et al. New H-mode regimes with small ELMs and high thermal confinement in the Joint European Torus. *Physics of Plasmas*, 29(3):032505, 2022.

[20] C. H. K. Chen, K. G. Klein, and G. G. Howes. Evidence for electron Landau damping in space plasma turbulence. *Nature Communications*, 10(1):1–8, 2019.

[21] S. A. Horvath, G. G. Howes, and A. J. McCubbin. Electron Landau damping of kinetic Alfvén waves in simulated magnetosheath turbulence. *Physics of Plasmas*, 27(10):102901, 2020.

[22] F. Jenko, W. Dorland, M. Kotschenreuther, and B. N. Rogers. Electron temperature gradient driven turbulence. *Physics of Plasmas*, 7(5):1904–1910, 2000.

[23] J. F. Artaud, V. Basiuk, F. Imbeaux, M. Schneider, J. Garcia, G. Giruzzi, P. Huynh, T. Aniel, F. Albajar, J.M. Ané, et al. The CRONOS suite of codes for integrated tokamak modelling. *Nuclear Fusion*, 50(4):043001, 2010.

[24] R. L. Miller, M.-S. Chu, J. M. Greene, Y. R. Lin-Liu, and R. E. Waltz. Noncircular, finite aspect ratio, local equilibrium model. *Physics of Plasmas*, 5(4):973–978, 1998.

[25] H. Doerk. *Gyrokinetic simulation of microtearing turbulence*. PhD thesis, Universität Ulm, 2013.

[26] F. L. Hinton and R. D. Hazeltine. Theory of plasma transport in toroidal confinement systems. *Reviews of Modern Physics*, 48(2):239, 1976.

[27] S. Moradi, I. Pusztai, I. Voitsekhovitch, L. Garzotti, C. Bourdelle, M. J. Pueschel, I. Lupelli, M. Romanelli, JET-EFDA Contributors, et al. Core micro-instability analysis of JET hybrid and baseline discharges with carbon wall. *Nuclear Fusion*, 54(12):123016, 2014.

[28] N. Kumar, Y. Camenen, S. Benkadda, C. Bourdelle, A. Loarte, A. R. Polevoi, F. Widmer, et al. Turbulent transport driven by kinetic ballooning modes in the inner core of JET hybrid H-modes. *Nuclear Fusion*, 61(3):036005, 2021.

[29] J. W. Connor, J. B. Taylor, and H. R. Wilson. Shear damping of drift waves in toroidal plasmas. *Physical Review Letters*, 70(12):1803, 1993.

[30] R. E. Waltz, R. L. Dewar, and X. Garbet. Theory and simulation of rotational shear stabilization of turbulence. *Physics of Plasmas*, 5(5):1784–1792, 1998.

[31] E. A. Belli and J. Candy. Fully electromagnetic gyrokinetic eigenmode analysis of high-beta shaped plasmas. *Physics of Plasmas*, 17(11):112314, 2010.

[32] M. J. Pueschel, M. Kammerer, and F. Jenko. Gyrokinetic turbulence simulations at high plasma beta. *Physics of Plasmas*, 15(10), 2008.

[33] M. Kammerer, F. Merz, and F. Jenko. Exceptional points in linear gyrokinetics. *Physics of Plasmas*, 15(5), 2008.

[34] B. J. Frei, A. C. D. Hoffmann, P. Ricci, S. Brunner, and Z. Tecchiolli. Moment-based approach to the flux-tube linear gyrokinetic model. *Journal of Plasma Physics*, 89(4):905890414, 2023.

[35] A. M. Dimits, G. Bateman, M. A. Beer, B. I. Cohen, W. Dorland, G. W. Hammett, C. Kim, J. E. Kinsey, M. Kotschenreuther, A. H. Kritz, et al. Comparisons and physics basis of tokamak transport models and turbulence simulations. *Physics of Plasmas*, 7(3):969–983, 2000.

[36] R.E. Waltz, G.D. Kerbel, and J. Milovich. Toroidal gyro-landau fluid model turbulence simulations in a nonlinear ballooning mode representation with radial modes. *Physics of Plasmas*, 1(7):2229–2244, 1994.

[37] F Romanelli. Ion temperature-gradient-driven modes and anomalous ion transport in tokamaks. *Physics of Fluids B: Plasma Physics*, 1(5):1018–1025, 1989.

[38] M. J. Pueschel, P. W. Terry, F. Jenko, D. R. Hatch, W. M. Nevins, T. Görler, and D. Told. Extreme heat fluxes in gyrokinetic simulations: a new critical β. *Physical Review Letters*, 110(15):155005, 2013.

[39] M. J. Pueschel, P. W. Terry, and D. R. Hatch. Aspects of the non-zonal transition. *Physics of Plasmas*, 21(5), 2014.

[40] D. R. Mikkelsen and W. Dorland. Dimits shift in realistic gyrokinetic plasma-turbulence simulations. *Physical Review Letters*, 101(13):135003, 2008.

[41] F. P. Orsitto et al. Study on differences of ECE and high resolution thomson scattering temperature measurements in DT (deuterium-tritium) plasmas on JET. In *49th EPS Conference on Plasma Physics, Bordeaux, France, 3-7 July 2023*, 2023.